2000

Atomic Force Microscopy Study of the Initial Stages of Anodic Oxidation of Aluminum in Phosphoric Acid Solution

Huiquan Wu
Iowa State University

Xiao Zhang
Iowa State University

Kurt R. Hebert
Iowa State University, krhebert@iastate.edu

Atomic Force Microscopy Study of the Initial Stages of Anodic Oxidation of Aluminum in Phosphoric Acid Solution

Abstract
Aluminum foils with two different surface topographic textures were anodically oxidized at constant current in a phosphoric acid bath. *In situ*atomic force microscopy (AFM) was used to follow the initial development of surface topography on a 1 μm scale, during the early stages of porous oxide film formation. Microscopic convex features such as ridges on both foils begin to increase in height and width when the anodic film thickness exceeds the initial feature height. Equations of a mathematical model are presented incorporating established interfacial reactions and oxide conduction behavior. The model indicates that the film-solution interface recedes into the metal during anodizing, since the current efficiency for oxide formation is smaller than the oxygen ion transport number in the film. Ridge surfaces increase in height due to the higher local conduction resistance to the film-solution interface, while film deposits rapidly at ridges because of the low local resistance to the metal-film interface. In agreement with the AFM results, enhanced oxide growth at ridges should start when the potential field in the film becomes two-dimensional, as a result of the film growing to a thickness larger than the ridge height.

Disciplines
Chemical Engineering

Comments
This article is from *Journal of the Electrochemical Society* 147 (2000): 2126–2132, doi:10.1149/1.1393496. Posted with permission.

Journal of The Electrochemical Society, **147** (6) 2126-2132 (2000)
S0013-4651(99)04-054-9 CCC: $7.00

Atomic Force Microscopy Study of the Initial Stages of Anodic Oxidation of Aluminum in Phosphoric Acid Solution

Huiquan Wu,* Xiao Zhang, and Kurt R. Hebert**

Department of Chemical Engineering, Iowa State University, Ames, Iowa 50011, USA

Aluminum foils with two different surface topographic textures were anodically oxidized at constant current in a phosphoric acid bath. *In situ* atomic force microscopy (AFM) was used to follow the initial development of surface topography on a 1 μm scale, during the early stages of porous oxide film formation. Microscopic convex features such as ridges on both foils begin to increase in height and width when the anodic film thickness exceeds the initial feature height. Equations of a mathematical model are presented incorporating established interfacial reactions and oxide conduction behavior. The model indicates that the film-solution interface recedes into the metal during anodizing, since the current efficiency for oxide formation is smaller than the oxygen ion transport number in the film. Ridge surfaces increase in height due to the higher local conduction resistance to the film-solution interface, while film deposits rapidly at ridges because of the low local resistance to the metal-film interface. In agreement with the AFM results, enhanced oxide growth at ridges should start when the potential field in the film becomes two-dimensional, as a result of the film growing to a thickness larger than the ridge height.

Manuscript submitted April 15, 1999; revised manuscript received February 4, 2000.

Anodic oxidation of aluminum in acidic solutions produces porous oxide films. When electropolished aluminum substrates are used, the pores in these films are on the order of 100 nm in diam, and are arranged in a two-dimensional hexagonal lattice.[1] Traditionally, the films have been used for corrosion protective coatings and surface finishing. In recent years, they have been increasingly explored as templates for nanostructures involving a variety of materials.[2-6] Experimental aspects of porous oxide growth and mechanistic explanations are reviewed by Thompson and Wood, Despic and Parkhutik, and Thompson.[7-9]

The developing morphology of porous oxide films was thoroughly characterized with transmission electron microscopy (TEM) by O'Sullivan and Wood, Furneaux *et al.*, and Shimizu *et al.*,[10-12] and correlated with transient potential or current measurements. For constant current anodizing, the potential, initially, increases at a nearly constant rate to a maximum of 10-200 V in a period of up to a few minutes, and then decreases to a constant value which is maintained during the anodizing period. The maximum potential depends on the anodizing bath composition. The electropolished aluminum substrates for these experiments are covered by a network of ridges on the order of 10 nm high. During the initial potential rise, the oxide grows on the entire metal surface, but most rapidly above these ridges. After the potential maximum, the oxidation current flows predominantly through the thinner film between the ridge sites, while the curved interface shape leads to the formation of new oxide beneath the thick film over the ridge sites. In this manner, deposition of the pore walls continues, while the length of the conduction path through the thin film at the pore bottoms remains constant.

According to this description, the eventual formation of a porous film is consequence of the film and interface geometry generated by rapid initial oxidation at pre-existing ridges. Thus, as Thompson and Wood recognized,[7] explaining this locally enhanced oxidation is a critical step toward an understanding of porous oxide growth. During the initial potential rise, the TEM studies show that growth of oxide on ridges continues to be preferred even after the length of the conduction path through the film on ridges is clearly greater than on the surface between them. Some investigators have given reasons that the film on ridges may be more conductive than elsewhere. Thompson and Wood suggested that the ridges may be sites of impurity segregation at the metal surface; oxide growth would then lead to stress in the film and cracking, and thus to locally rapid conduction.[7] Macdonald hypothesized that the film on the ridges may contain a high concentration of point defects such as vacancies, accounting for a large local cation flux through the film during oxidation.[13] Parkhutik and co-workers considered the effect of film geometry on the local conduction rate to be the factor responsible for porous oxide formation, and supported this view with model calculations.[14,15] In the mechanism of Shimizu *et al.*, the buildup of tensile stress in the film as it grows above ridges leads to the formation of cracks which continue to serve as conductive pathways during film growth.[12]

To discriminate between different hypotheses for ridge oxidation, studies of porous oxide formation on electrodes with different morphologies than electropolished aluminum would be useful. Few such investigations have been reported. Thompson *et al.* observed enhanced oxide growth near scratches,[16] while Jessensky *et al.*[5] found that highly ordered porous layer morphologies could not be obtained on foils which had not been electropolished.[5] In the present investigation, an *in situ* atomic force microscopy (AFM) study was carried out of anodic oxide growth on aluminum in phosphoric acid. The electrodes used in some of the experiments were high purity aluminum foils which had received no treatment prior to oxidation, and which contained topographic features as small as tens of nanometers. Other experiments made use of foils subjected to dissolution under cathodic polarization in an electropolishing solution. This treatment resulted in a scalloped topography like that after electropolishing, but which could be imaged more readily on a micrometer scale due to the larger ridge size. With *in situ* AFM, shape changes of the various individual features were observed during oxidation, and on this basis the effect of local geometry on oxide growth is characterized. A mathematical model for the development of the porous oxide morphology is then presented.

Experimental

Aluminum samples were 99.98% purity annealed foils, about 100 μm thick. The typical grain size was also 100 μm. The foils were high cubicity type, indicating a high proportion of surface grains having (100) orientation. Solutions were prepared from reagent grade chemicals and distilled and deionized water. Disks of 15 mm diam were cut from the foil for use as electrodes. The cathodic dissolution surface preparation was carried out by applying a cathodic current density of 5 mA/cm^2 for 2 min, in an electropolishing solution composed of phosphoric acid, ethanol, and water in a volume ratio of 40:38:25 at 40°C.

Anodic oxidation at a constant applied current density of 5 mA/cm^2 was carried out at room temperature in the fluid cell of the AFM system (Digital Instruments Nanoscope III). The foils were bonded to steel sample pucks with conductive silver paint (GC Elec-

* Electrochemical Society Student Member.
** Electrochemical Society Active Member.

S0013-4651(99)04-054-9 CCC: $7.00

tronics), and placed on the AFM scanner head. The fluid cell was modified for electrochemical experiments by addition of liquid reservoirs to the fluid inlet and outlet ports of the cell. An 0.85 mm diam Pt wire placed in one of the reservoirs served as the counter electrode. The other reservoir, mounted higher than the cell, was filled with cell electrolyte solution (1 M H_3PO_4) which flowed into the cell to replace any leakage. A 0.3 mm diam Pt wire used as a reference electrode was inserted into the cell through a small hole. A potentiostat (PAR 273) was used to supply electrochemical polarization, and a voltmeter (Keithley 194A) collected the potential data in the galvanostatic anodizing experiments. Electrical connection between the aluminum foil (working electrode) and the potentiostat was made with a thin piece of Al foil placed between the sample puck and the AFM scanner head. Teflon tape was used to seal the cell on the scanner head and block leakage. The volume of cell electrolyte solution was about 0.2 mL. The pH of the cell solution was initially close to 1, and measurements with pH paper indicated that it did not change significantly as a result of anodizing. Other anodizing experiments were carried out using the same current density, but in a beaker containing several hundred milliliters of 1 M H_3PO_4 solution.

A 14 μm scanner was used for imaging, along with Si cantilevers (Si_3N_4 tip). The photodiode set point voltage was set at 2.39 V. Using the cantilever spring constant of 0.06 N/m, the applied force is estimated to be 0.8 nN. Images were compiled continuously during dissolution. Each image was 5 × 5 μm size, composed of 256 pixels in each direction. Frames were captured at a rate of 65 s per image; the scan time per line in the fast scan direction was 10.25 s. The microscope was calibrated using a grid with height 25 nm and spacing 1 μm. Image files were exported to the Image SXM software application for calculation of curvature images and local height differences between images. Further details of the experimental procedure are given by Zhang.[17] For all images in the paper, the AFM software was used to fit a quadratic reference surface parallel to the *x* (horizontal) axis images, and then subtract this surface from them. This "planefitting" procedure removed bowing of the sample in the *y* direction. The AFM software was also used for calculation of surface roughness.

Results and Discussion

Potential transients.—The potential transients measured during anodic oxidation in the AFM fluid cell are shown in Fig. 1. The transients are nearly the same shape for the as-received foil and cathodically treated foil in the AFM cell, as well as as-received foil in a beaker with a large volume of solution. The initial potential in the AFM cell is about 5 V higher than in the beaker, probably the result of a higher cell ohmic resistance. The potential during anodizing at first increases nearly linearly at 52 V/min to a peak value of 71-73 V at 95-118 s, then decreases to 62 V at 200-240 s, and then remains constant or increases slowly for the rest of the anodizing period. Parkhutik and Shimizu *et al*. have found potential transients of similar shapes for in 0.4 M H_3PO_4 and electropolished aluminum, using the same applied current density of 5 mA/cm^2 as in this work.[12,18] The transient of Shimizu has a larger peak potential of 150 V at 120 s. The current efficiency for oxide formation during the initial linear increase is estimated to be 35%, by dividing the slope of the transient by 147 V/min, the slope expected for 100% current efficiency.[12] This value is significantly smaller than with the 54% efficiency calculated by Shimizu, perhaps due to the lower pH of the 1 M H_3PO_4 anodizing bath used here. Nevertheless, the potential transients in Fig. 1 are of the characteristic shape established by prior work, and are not influenced significantly by the AFM cell.

Images during anodic oxidation of as-received foil.—AFM images were acquired continuously during the oxidation experiments in Fig 1. Figure 2 shows a selection of the top view images obtained during oxidation of the as-received foil. The figure shows the same 3 × 3 μm areas, cropped from the original 5 μm images. Image a represents the foil surface on open circuit just prior to application of the current, while images b-d were taken during the period of applied current. The mean times during capture of images b-d are marked on the potential transients in Fig. 1; image capture would have begun 32.5 s before, and ended 32.5 s after these times. In the top view images, the surface height is expressed by a gray scale where lighter tones correspond to higher elevations. The topography is also depicted by section profiles and curvature images in Fig. 3 and 4. The section profiles in Fig. 3a show the height along a ridge, while those in Fig. 3b give the height variation in the direction perpendicular to the ridges (see lines marked in Fig. 2a). The curvature

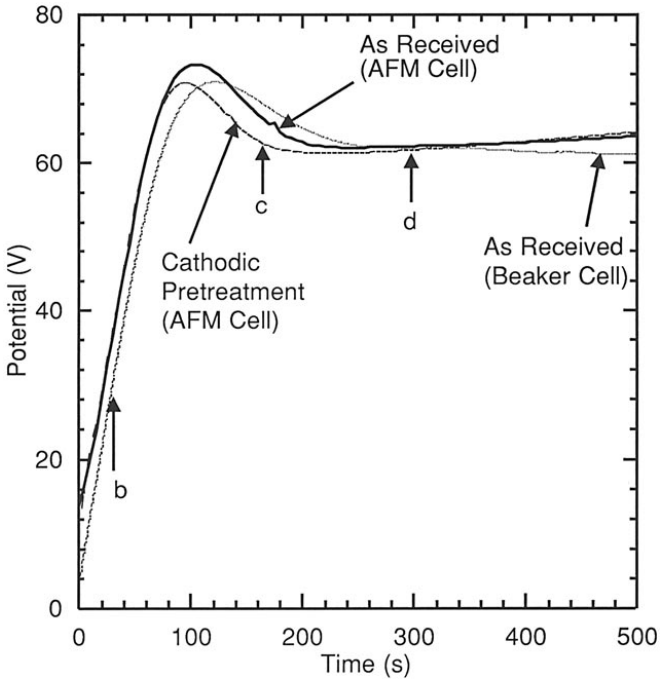

Figure 1. Potential transients measured during anodic oxidation of aluminum samples in the AFM fluid cell. Arrows mark the average times during the capture of images b, c, and d in Fig. 2-5.

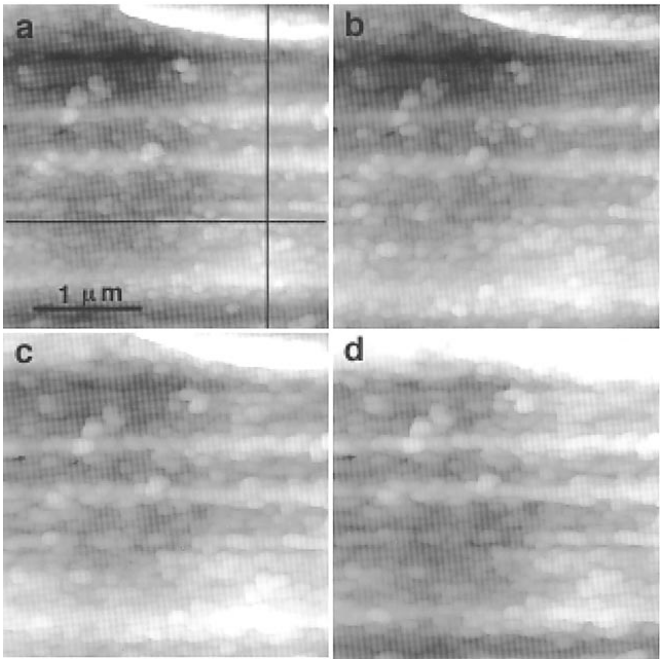

Figure 2. AFM top view images during oxidation of as-received aluminum foil. Image a was captured at open circuit just before current application, and images b-d were obtained during oxidation, at mean times indicated in Fig. 1. Slow scan directions are up for a and down for b-d. Maximum height contrast 100 nm for all images.

S0013-4651(99)04-054-9 CCC: $7.00

images in Fig. 4 show the shapes of small convex features more clearly than do the top view images. The curvature at each pixel was calculated by applying a finite difference formula which approximates the mathematical definition of the curvature, averaged over a square area 98 nm wide. The curvature calculation acts as a high-pass filter on the height image, as it emphasizes the edges of small convex features, but loses information about height variations on a length scale on the order of 1 μm.

Taken together, Fig. 2-4 describe the surface morphology changes due to oxidation. As reported by Scherer *et al.*, the foil surface is initially covered with platelet like features about 100 nm in size, which form parallel rows.[19] Some of these rows, spaced at intervals of roughly 200-500 nm, are elevated by 20-50 nm and constitute small ridges. While the images represent the ridges along the fast scan direction, their presence in images does not depend on the orientation of the sample surface. The platelet and ridge texture may result from thermal faceting during annealing, and the rolling operation. Some of the platelets project above their neighbors as "hills" typically 100-200 nm wide and 5-10 nm high. The section profiles in Fig. 3a emphasize the topography due to the hills, while those in Fig. 3b are determined by the ridges. Comparison of the open-circuit curvature images (Fig. 4) and horizontal section profiles (Fig. 3a) with the first ones during oxidation shows that nearly all hills increase in width. Changes in hill heights between images a and b are also shown as a histogram in Fig. 5. In the figure, the local height of a hill is defined as the difference between its height and the minimum height of the immediately adjacent surface around it. The horizontal axis represents the local height difference of individual hills between images a and b. Figure 5 shows that nearly all the hills increased in height due to oxidation, with the average height increase 3.7 nm. The apparent reduction of height of some hills was due to the neighboring hills increasing in width until they touched it, which increased the height of the reference surface used to calculate the local height. Figures 3a and 4 show that growth of hills continues between images b and c, which was captured during the time of the potential peak in Fig. 1. Lateral growth results in merging of some adjacent larger hills. However, the predominant topographic change from image b to c is the increase in height and width of ridges, as shown in Fig. 2 and 3b. After the potential peak, the topography change is relatively small (Fig. 2-4c and d). This is expected, since the TEM studies have shown that the peak potential marks the beginning of steady-state porous oxide growth, during which the film is extended by new oxide only at the metal-film interface. No "pores" in the film can be seen in the images, since the AFM scanning tip cannot effectively contact the surface of the small spaces between the ridges, where the pores may be found.

The analysis of the images of as-received foil indicates that nearly all microscopic convex features grow in height and width as a result of anodizing. According to the potential transient in Fig. 1, the average potentials during images b and c are about 28 and 65 V, respectively. Growth on hills appears to predominate at earlier times and at low voltage, and that on ridges later and at high voltage. The TEM images of Shimizu *et al.* suggest a film thickness to voltage ratio of about

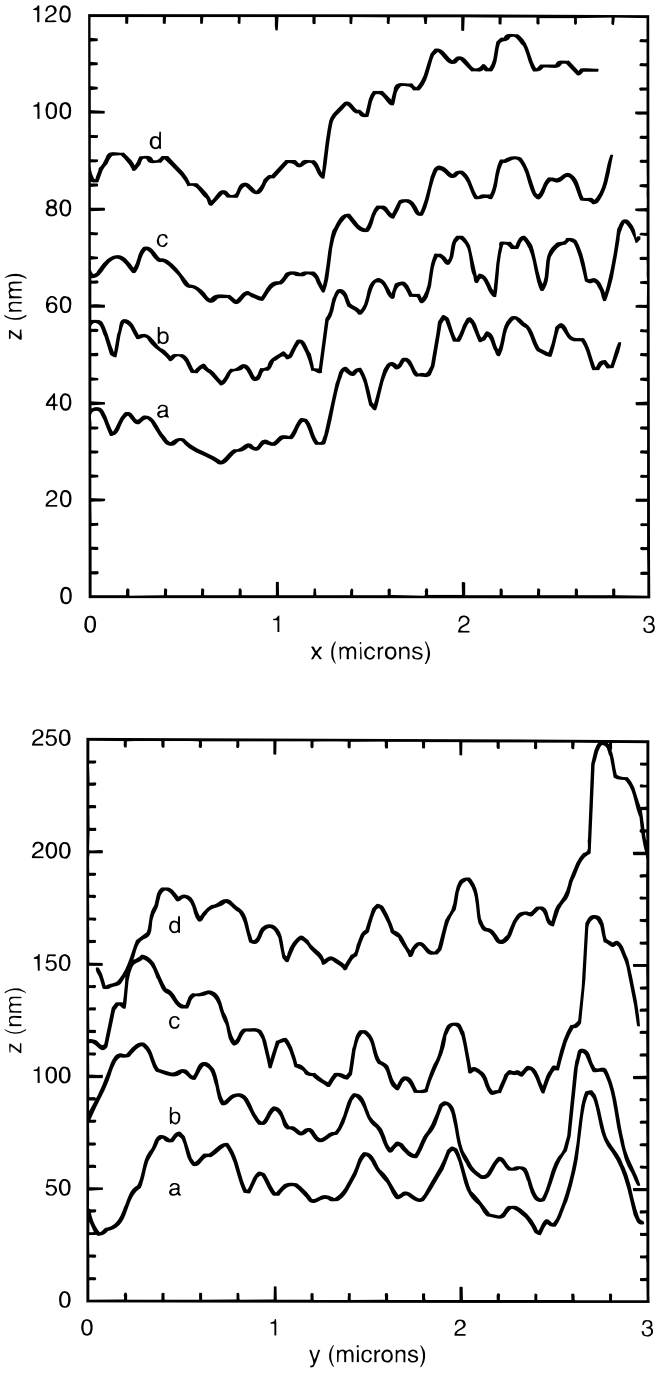

Figure 3. Elevation profiles during oxidation of as-received foil, along the (a) horizontal and (b) vertical lines in Fig. 2a. Profiles are offset for clarity of presentation.

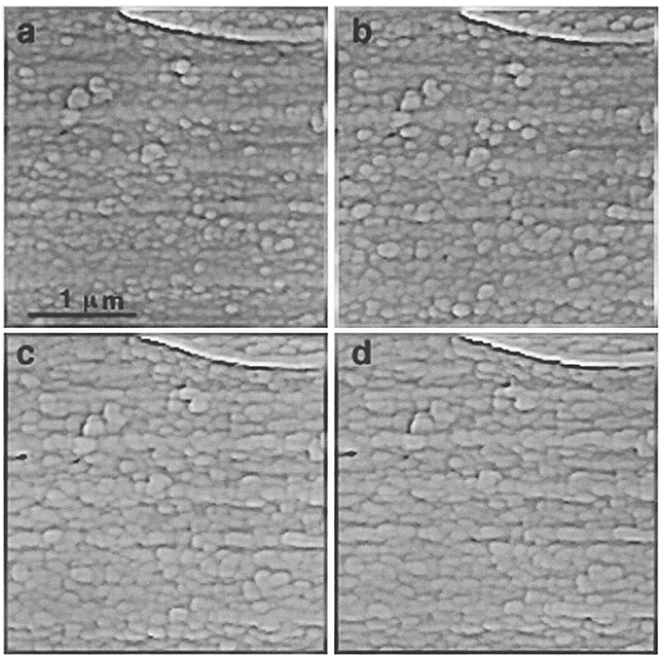

Figure 4. Curvature images corresponding to the top view images in Fig. 2.

S0013-4651(99)04-054-9 CCC: $7.00

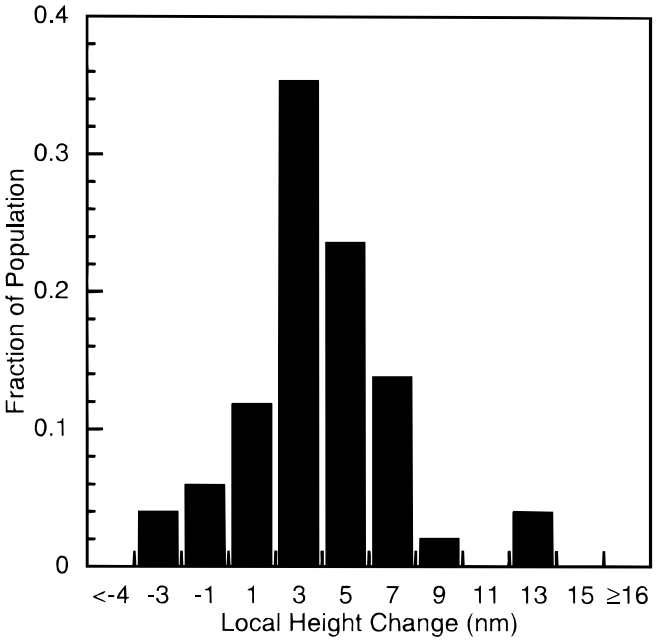

Figure 5. Histogram showing the distribution of local height changes of small convex surface features on as-received foil, between the open-circuit image (Fig. 2a) and the first image acquired during oxidation (Fig. 2b). The local height of a surface feature (hill) is its height relative to the minimum height of the surface immediately around the hill. The histogram includes 51 hills in the lower 1 μm of Fig. 2.

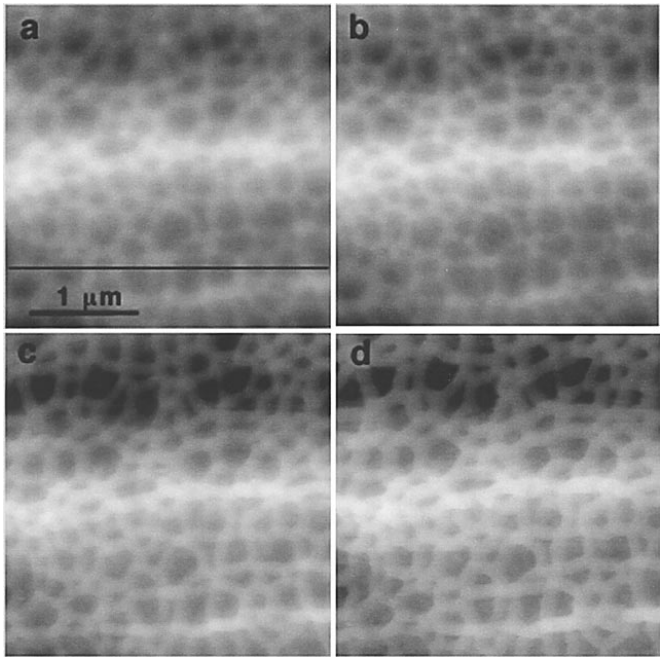

Figure 6. AFM top view images during oxidation of foil pretreated by cathodic dissolution. Image a was captured at open circuit just before current application, and images b-d were obtained during oxidation, at mean times indicated in Fig. 1. Slow scan directions are down for a and up for b-d. Maximum height contrast 200 nm for all images.

1.2 nm/V, [12] so that the average anodic film thickness after images b and c should be about 35 and 80 nm. As stated above, the typical hill and ridge heights are 5-10 nm and 20-50 nm, respectively. Hence, the onset of growth of either hills or ridges appears to correspond to the anodic film thickness becoming larger than the size of that feature. Enhanced growth of hills continues until the film surface on individual hills merges to form continuous ridges. Growth of ridges is stopped by the transition to steady-state porous film formation.

The growth of anodic oxide on the as-received foil, and on the cathodically pretreated foil as well, may be influenced by the scanning action of the AFM tip. Guay and co-workers,[20,21] as well as Schmutz and Frankel,[22,23] found that the corrosion rate of aluminum in NaCl solution is enhanced by the tip, as evidenced by a recessed scan area relative to the surrounding surface. To detect a possible tip effect on oxidation, foil was anodized for 200 s in a beaker cell and then imaged in air. The images appear qualitatively similar to those in the AFM cell, and the section profiles reveal similar ridge and hill heights as in Fig. 3 at the same anodizing time. The lack of a tip effect may be understood, since in the present work, the estimated tip sample force is 0.8 nN, about an order of magnitude smaller compared to forces needed to produce tip enhanced dissolution.[21] In fact, Martin *et al*. imaged aluminum during open-circuit dissolution, using the same solution and the same applied tip sample force as the present work, and did not observe that the scanned area was recessed.[24]

Images during oxidation of cathodically pretreated foil.—Figure 6 shows the four top view images during anodic oxidation of the cathodically pretreated aluminum foil. Image a was acquired just before anodizing, while images b-d were taken under the applied current, at the mean times indicated in Fig. 1. Section profiles along the line marked in Fig. 6a are found in Fig. 7, and represent typical heights of the surface features. The initial topography in Fig. 6a, consisting of roughly circular scallops separated by ridges, is typical of that left on aluminum by a number of dissolution processes in different media. The ridge heights are typically about 10-30 nm, and the scallops are about 200-400 nm wide. Hence, the ridges have roughly the same height and spacing as the parallel ridges on as-received foil. Very little change of ridge height or width is evident between the open-circuit image and the first one during oxidation (Fig. 6, 7a, and b). However, between images b and c, the latter at a time during the potential peak, Fig. 6 and 7 show that the ridge heights increase by 10-20 nm, and their widths increase by as much as 50 nm. From image c to image d at a time after the potential maximum, there is no significant height or width increase. These trends of surface development are similar to those on as-received foils, in that the primary convex features, *i.e.*, ridges, grow in height and

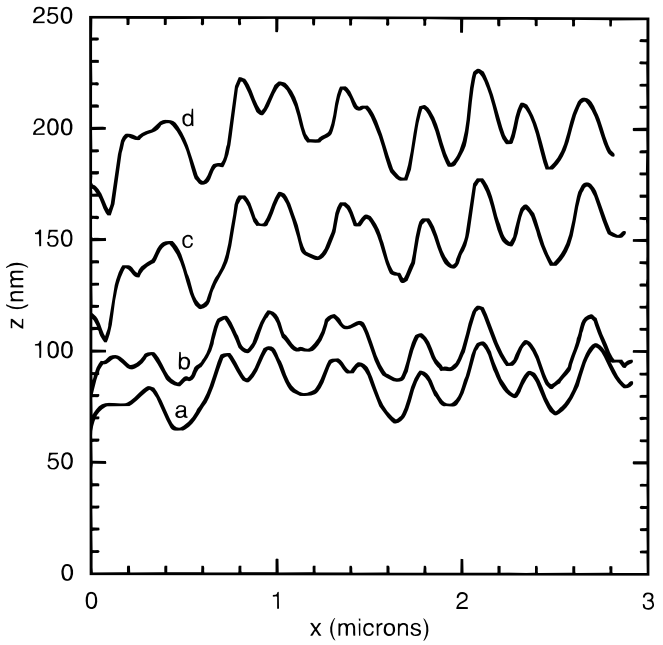

Figure 7. Elevation profiles during oxidation of cathodically treated foil, at the location of the horizontal line drawn in Fig. 6a. Profiles are offset for clarity of presentation; the *z* scale indicates relative heights along individual profiles, not absolute heights.

S0013-4651(99)04-054-9 CCC: $7.00

width. The anodizing voltage equivalent to the size of the larger ridges, about 30 nm, is 40 V. From Fig. 1, growth of ridges occurs when the voltage is larger than this value. Therefore, the same geometric rule proposed for as-received foil holds here, that a convex feature begins to grow when the film reaches a thickness greater than the feature size. The growth of ridges in the present experiments is less dramatic than that found in the TEM studies,[7,12] possibly the result of the lower current efficiency for oxide formation.

Comparison of the two surface types.—The morphology changes on both types of surface during the entire anodizing period are indicated in Fig. 8, which shows the transient development of the root-mean-square (rms) surface roughness. The rms roughness is equivalent to the standard deviation of the height. It was calculated using the same 2×2 μm area on each image of either as-received or cathodically treated foils. Roughness data for other images in addition to those in Fig. 2 and 6 are shown. For both aluminum samples, the roughness increases sharply up to the time of 200 s, just after the potential peak at the beginning of the constant potential period. The largest roughness increase is from the peak time of about 100 to 200 s, when ridge growth on either foil is the predominant topographic change. The total roughness increase up to 200 s is about twice as large on the cathodically treated foil compared to the as-received foil, the same as the ratio of initial roughness of the two surfaces. As noted above, the typical ridge height and spacing is similar between the two foils, but ridges on the as-received foil run only horizontally in the images, while those on the cathodically pretreated foil run both horizontally and vertically. Thus, the ridge length per unit area is about two times larger on the cathodically treated foil, which is believed to explain the ratios of initial roughness and roughness change. For comparable potentials, the oxide growth rate on ridges is similar on both as-received and cathodically treated foil. After the peak, there was no further change on the cathodically pretreated foil, while the more extensive data on the as-received foil show that the roughness decreases slowly. The slow decrease at long times was due to the ridge tops becoming smoother and wider. For electropolished aluminum, the same coarsening of the oxide's outer surface is found, and can be explained by slow dissolution of the outer portion of the film in the acid anodizing bath.[25]

In the present experiments as well as for electropolished aluminum, the initial topography development during anodizing is characterized by rapid growth of convex features, whether hills or ridges. For as-received foils, the topography results from the thermomechanical processing of the foils, while the ridges on the cathodically pretreated foil are the product of surface dissolution. Despite these differences in their origin, ridges on the two foils grow at comparable rates. Also, for both foils, the images suggest the same geometric criterion for enhanced growth of convex features: that the film thickness exceeds the feature size. This conclusion would indicate that the progress of oxidation on convex features is determined primarily by geometric factors, as opposed to special properties of these sites related to the processing conditions. In the next section, a model is described which explores the influences of geometry on the local conduction and dissolution rates.

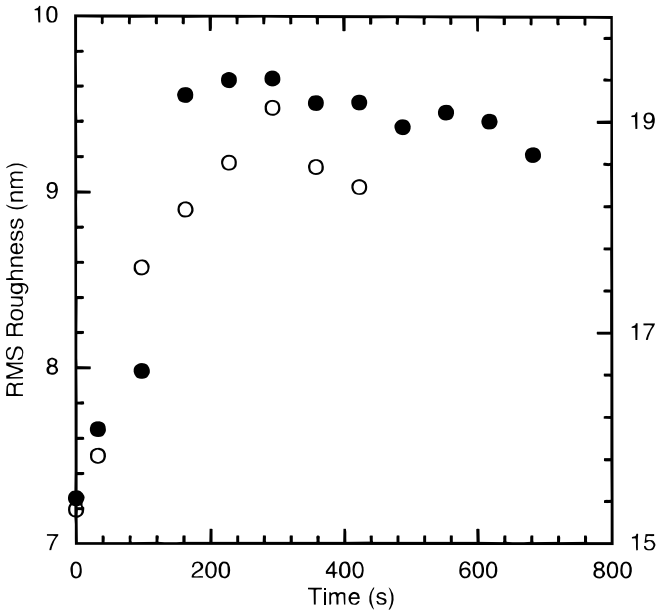

Figure 8. RMS surface roughness as a function of time during anodic oxidation experiments. Filled symbols (left axis) are for as-received foil, while open symbols (right axis) represent cathodically treated foil

Mathematical model for oxidation.—In this section, the equations of a mathematical model for oxide growth are presented. No calculation results are given, but the anticipated predictions of film morphology evolution during anodizing are discussed.

In the past, a variety of chemical and physical processes have been suggested to be responsible for the unique porous layer morphology. The earliest mechanisms for porous oxide growth considered that the formation and chemical dissolution of oxide occur simultaneously, and hence, the pore volume would be the result of oxide dissolution. However, since the dissolution rate of oxide material in anodizing solutions is much smaller than that of oxide formation, several factors were suggested to account for accelerated dissolution in the pores. These include Joule heating by the electric current,[26] and the action of the electric field.[18,27] Nagayama, Siejka, and their co-workers disputed pore formation by chemical oxide dissolution.[28-31] Cherki and Siejka established, using O^{18} tracer measurements, that the rate of oxide dissolution during anodizing is much too small to account for the pore volume, and concluded that the porous oxide structure forms directly by oxidation.[30,31] These authors identified the reactions at the film-solution interface as ion-transfer processes: (*i*) the formation of oxygen ions in the film from water in solution, *i.e.*, H_2O (aq) $\leftrightarrow O^{-2}$ (f) + $2H^+$ (aq); and (*ii*) the dissolution of aluminum ions in the film, *i.e.*, Al^{+3} (f) $\rightarrow Al^{+3}$ (aq). As shown by Våland and Heusler, these same interfacial reactions predominate over the entire pH range from acid to alkaline solutions.[32] Thus, the present model takes the point of view that no special interfacial processes participate in formation of porous oxide layers.

The model equations are based on the established conduction behavior of anodic films and the interfacial reactions. Figure 9 shows the outline of the cross section of an anodic film formed to 50 V at 5 mA/cm^2 in a 0.4 M H_3PO_4 solution, from one of a sequence of TEM micrographs.[12] It represents a relatively early time during the increase of the potential to the peak value of 150 V and is used to define the model coordinate system. At subsequent times, continuing enlargement of the peaks on the oxide surface occurs. The potential field in the film $\phi(x,y)$ obeys the equation for charge conservation in the oxide which assumes no space charge

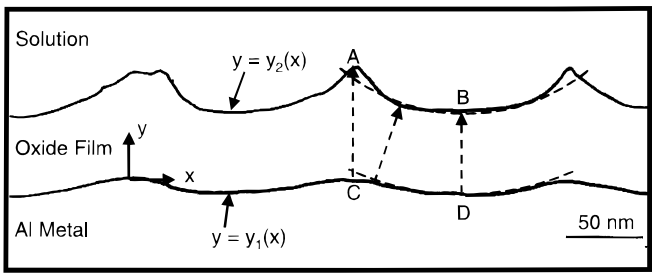

Figure 9. Outline of cross section of anodic oxide film formed to a potential of 50 V at an applied current density of 5 mA/cm^2 in 0.4 M H_3PO_4, from TEM micrograph.[31] Dashed curves are concentric circular arcs, and dashed vectors represent local current paths through the film. Other symbols are explained in the text.

S0013-4651(99)04-054-9 CCC: $7.00

$$\nabla\cdot\kappa\tilde{E} = 0 \qquad [1]$$

where $\tilde{E} = -\nabla\phi$ and for high-field conduction the conductivity κ is given by

$$\kappa = \frac{i_{a0}}{|\tilde{E}|}\exp\left(B|\tilde{E}|\right) \qquad [2]$$

i_{a0} and B are the conduction parameters found in the experimentally derived expression for the conduction current density in one-dimensional films, *i.e.*, $i = i_{a0}\exp(BE)$. The origin of the *x-y* coordinate system implied in Eq. 1 is stationary. Phosphate anions are incorporated into anodic films, suggesting that space charge effects might be important.[18] However, Skeldon *et al*. have shown that the transport of a variety of incorporated anions in barrier anodic films is characterized by the movement of uniform migration fronts, indicating that, at least at the incorporation levels of their work, the electric field is uniform and therefore space charge is not significant.[33] A possible explanation is that other charged defects such as oxygen vacancies can at least partly compensate for the incorporated anion charge. In any case, this is the motivation for the assumption of no space charge in Eq. 1.

While the film grows, the inner interface at $y_1(x,t)$ moves inward as metal is consumed. The vector interface velocity is determined by a balance on oxygen ions[34]

$$\tilde{v}_1\cdot\tilde{n}_1 = \frac{\dfrac{\partial y_1}{\partial t}}{\sqrt{1+\left(\dfrac{\partial y_1}{\partial x}\right)^2}} = -\frac{t_O}{6FC_{ox}}\tilde{i}\cdot\tilde{n}_1 \qquad [3]$$

where $\tilde{n}_1$ is the unit normal vector at the interface pointing into the oxide. The first equality assumes a two-dimensional geometry, as in the figure.[35] The current density carried by oxygen ions is $t_O\tilde{i}$, where t_O is the oxygen ion transport number. The motion of the film-solution interface is governed by

$$\tilde{v}_2\cdot\tilde{n}_2 = \frac{\dfrac{\partial y_2}{\partial t}}{\sqrt{1+\left(\dfrac{\partial y_2}{\partial x}\right)^2}} = \frac{\epsilon - t_O}{6FC_{ox}}\tilde{i}\cdot\tilde{n}_2 \qquad [4]$$

where the unit normal vector, $\tilde{n}_2$, points into the solution. The current density of oxygen ion transport into the film is $t_O\tilde{i}$, while the current density of oxygen ion formation at the film surface is $\epsilon\tilde{i}$. ϵ is the current efficiency for film growth, defined by $i_L/(i_c + i_L)$, in which i_c and i_L are the current densities of metal and oxygen ion transfer processes, respectively, at the film-solution interface. The boundary condition at the metal-film interface, $y_1(x)$, is

$$\phi[y_1(x)] = E_i + v_R t - E^0_{Al/Al_2O_3} \qquad [5]$$

and at the film-solution interface, $y_2(x)$, $\phi = 0$.

The model equations along with the interface profiles in Fig. 9 are now used to explain the development of the film morphology at later times. According to Thompson, the condition $\epsilon < t_O$ is typically found during porous oxide formation.[9] For example, for the conditions of Fig. 9, ϵ is 0.54,[12] and studies of barrier-type anodic films indicate $t_O = 0.6$.[9] In the present work, ϵ is 0.35. ϵ smaller than t_O implies that the rate of migration of oxygen ions into the film exceeds their deposition rate from solution, so that the film-solution interface moves in the negative *y* direction. From Eq. 3 and 4, the local interface velocities depend on the normal component of the current density, and thus on the local conduction resistance. The resistance is in turn determined by both the conduction path length and the interface geometry. The figure shows that between ridges, both these interfaces are well approximated as concentric circular arcs, and hence, the length of the current path (indicated by dashed vectors) is nearly uniform and smaller than that at ridges (*i.e.*, the distance BD is less than distance AC). Moreover, the sharply concave film geometry at A promotes restriction of the current lines in the oxide and a high local resistance, while the convex geometry at B produces spreading of the current lines and a low resistance. Thus, the resistance to A is greater than that to B, so that A should move more slowly than B, *i.e.*, the ridge height at the oxide surface increases. While A and C have the same conduction path length, the resistance to C is smaller owing to the local interface shape. For this reason, and because it is larger than ϵ^- C moves faster than A and the film thickness on the ridge increases. The relative velocities of C and D are less clear since conduction path length favors a higher resistance at C, while local interface shape suggests a lower resistance. However, at least the predictions of increasing ridge height and film thickness on the ridge are consistent with trends from TEM studies,[7,12] and support the validity of applying current distribution concepts to explain the morphology development.

The initial stages of anodic film growth can be described. At the outset of anodizing, the film thickness is smaller than the heights of surface features, and thus, the potential field in the film is one-dimensional: film growth is uniform over both ridges and valleys. However, when the film thickness becomes comparable to the ridge heights, the potential field is two-dimensional, and as argued above the interface shape effect enhances the current flux at points such as C relative to other sites at the metal-film interface. Similarly, the interface shape causes the current flux to points such as A to be reduced compared to both C and other points on the film surface. As a result, the ridge height on the film surface increases and the film thickness on the ridge builds up. Thus, the model explains the AFM observation that ridge growth becomes apparent after the film thickness exceeds the ridge height. At the metal-film interface, ridge points such as C can perhaps move at the same velocity as points such as D, as long as the interface at C remains sharply convex, and thus, the interface shape effect at C compensates for the longer conduction path. Eventually, though, the interface at C is flattened by consumption of metal; then, the resistance to C clearly exceeds that to D, D begins to move faster than C, and the metal-film interface becomes more and more deeply scalloped. The TEM micrograph sequence of Thompson and Wood clearly support this prediction: at first the preexisting ridges at the metal-film interface flatten while the film grows above them more rapidly than elsewhere, and later the interface between the ridges becomes deeply scalloped.[7]

As the depth of scallops at both interfaces increases, the interface shapes evolve to the nearly concentric, hemispherical contours found at the pore bottoms during steady-state porous oxide growth.[7] The second equality of Eq. 3 (modified for a three-dimensional geometry) is then

$$\frac{\partial y_1}{\partial t}\sqrt{1-\sin^2\theta} = -\frac{t_O i_r}{6FC_{ox}} \qquad [6]$$

Here, θ is the angle measured from the direction BD in the figure, with $\theta = 0°$ pointing downward and $\theta = 90°$ horizontally. i_r is the radial component of the current density at the metal-film interface. The square root factor in Eq. 6 is at least 0.90 for θ smaller than 25°. Hence, only a 10% decrease of i_r from its value at the midpoint between ridges is sufficient to keep $\partial y_1/\partial t$ constant up to a fairly large angle of 25°. Given the high sensitivity of the high-field conduction rate to the electric field, this current density variation can be achieved with only a small increase of oxide film thickness over this range of θ. With a uniform $\partial y_1/\partial t$, the shape of the metal-film interface is invariant with time, and thus, the interface shape would stop evolving when this nearly hemispherical contour is achieved. The transition to steady-state porous oxide growth can therefore be explained on this basis. Also, the present mechanism explains the peaked shape of the potential transient, as in Fig. 1. Since the growth of the scallops to the steady-state shape significantly increases the metal surface area, it is necessary that the potential decrease in order to maintain the constant applied current density. Scallop growth should then occur during the decrease of the potential to the steady-state value, as the

S0013-4651(99)04-054-9 CCC: $7.00

TEM studies indicate.[7] The large rms roughness increase in Fig. 8 which occurs during the declining potential period can be attributed to scallop growth.

As discussed earlier, previous models have proposed special processes to explain the porous film morphology, *e.g.*, field-assisted dissolution, localized cracking at the film-solution interface, high local concentrations of point defects, anionic space charge, and Joule heating, among others. To the authors' knowledge, none of these concepts have been tested by developing them mathematically as predictive models of the interface shape. In contrast, the present model uses established concepts of conduction, current distribution, and interface motion, which are easily formulated as equations. It has been shown that the present equations imply at least qualitatively aspects of the development of the film morphology revealed by microscopy studies, including the approach to a steady-state interface profile. Further calculations are needed to verify these predictions in quantitative terms.

Conclusions

In this work, anodic oxide growth on aluminum in phosphoric acid was investigated using *in situ* AFM. Both as-received and cathodically treated foils, which had different surface morphologies before anodizing, were used as substrates for film growth. The topography of the cathodically treated foil consists of a pattern of circular scallop-shaped depressions bordered by ridges. The as-received foil contains parallel ridges produced by rolling as well as smaller, projecting circular hills which are possibly thermal facets formed by annealing. On both foils, the ridge heights are 10-50 nm and their spacing is 200-500 nm; the hills are 100-200 nm wide and 5-10 nm high. During the initial period of anodizing at constant applied current, the apparent heights and widths or all hills and ridges increase, while at the same time the oxide thickness increases at a constant rate. The time at which a type of surface feature begins to grow corresponds to the oxide having reached a thickness comparable to the feature height.

The equations of a mathematical model are presented which describe conduction in the oxide film and interfacial reactions. On the basis of these equations, a mechanism explaining the observed topography evolution is given. During anodizing in acid, since the current efficiency for oxide formation at the film-solution interface is smaller than the oxygen ion transport number in the film, this interface recedes into the metal. When the film thickness exceeds the surface feature height, the potential distribution in the film becomes two-dimensional. The surfaces of ridges begin to move more slowly than points on valleys, because of the higher local conduction resistance to ridges. Moreover, the relatively low resistance to points at the metal-film interface beneath ridges causes the oxide film there to at first grow at an enhanced rate. However, when the interface below ridges becomes flat, points between ridges starts to move more rapidly, resulting in pronounced scalloping of the interface. It is suggested that a time-invariant interface morphology can be reached when the metal-film and film-solution interfaces between ridges becomes nearly concentric hemispherical contours. Therefore, the evolution of the porous oxide morphology can be explained at least in qualitative terms with consideration of current distribution effects coupled with equations describing interface motion. In this way, the present model contrasts with previous attempts to explain the film morphology, which have invoked a variety of special processes for that purpose.

Acknowledgments

Financial support for this work was provided by the National Science Foundation through grant DMR 9307308. Aluminum foils were donated by KDK Corp.

List of Symbols

B	field coefficient for conduction
C_{ox}	Al_2O_3 concentration in oxide film, mol/cm^3
$\tilde{E}$	electric field, V/cm
E_i	initial potential during anodizing, V *vs*. NHE
E^o_{Al/Al_2O_3}	equilibrium potential for formation of Al_2O_3, V *vs*. NHE
F	Faraday constant, 96487 C/equiv
i_{ao}	pre-exponential current densities for conduction, A/cm^2
$\tilde{i}$	conduction current density in oxide, A/cm^2
$\tilde{n}_1$, $\tilde{n}_2$	unit normal vectors at metal-film and film-solution interfaces, cm
t	time, s
t_O	transport number of oxygen ions in film
v_R	rate of potential increase during anodizing, V/s
$\tilde{v}_1$, $\tilde{v}_2$	velocities of metal-film and film-solution interfaces, cm/s
x, y	spatial coordinates, cm
y_1, y_2	positions of metal-film and film-solution interfaces of oxide film with respect to stationary coordinates, cm

Greek

ϵ	current efficiency for oxide growth
ϕ	potential in oxide film, V
κ	conductivity of oxide film, $(\Omega\text{-cm})^{-1}$

References

1. H. Masuda and K. Fukuda, *Science*, **268**, 1466 (1995).
2. D. Routkevitch, T. Bigioni, M. Moskovits, and J. M. Xu, *J. Phys. Chem.*, **100**, 14037 (1996).
3. P. Hoyer and H. Masuda, *J. Mater. Sci. Lett.*, **15**, 1228 (1996).
4. P. Hoyer, K. Nishio, and H. Masuda, *Thin Solid Films*, **286**, 88 (1996).
5. O. Jessensky, F. Müller, and U. Gösele, *J. Electrochem. Soc.*, **145**, 3735 (1998).
6. O. Jessensky, F. Müller, and U. Gösele, *Appl. Phys. Lett.*, **72**, 1173 (1998).
7. G. E. Thompson and G. C. Wood, in *Treatise on Materials Science and Technology*, Vol. 23, J. C. Scully, Editor, p. 253, Academic Press, New York (1983).
8. A. Despic and V. P. Parkhutik, in *Modern Aspects of Electrochemistry*, Vol. 20, J. O'M. Bockris, R. E. White, and B. E. Conway, Editors, Plenum Publishing, New York (1989).
9. G. E. Thompson, *Thin Solid Films*, **297**, 192 (1997).
10. J. P. O'Sullivan and G. C. Wood, *Proc. R. Soc. London*, **A317**, 511 (1970).
11. R. C. Furneaux, G. E. Thompson, and G. C. Wood, *Corros. Sci.*, **18**, 853 (1978).
12. K. Shimizu, K. Kobayashi, G. E. Thompson, and G. C. Wood, *Philos. Mag. A*, **66**, 643 (1992).
13. D. D. Macdonald, *J. Electrochem. Soc.*, **140**, L27 (1993).
14. V. P. Parkhutik and V. I. Shershulsky, *J. Phys. D: Appl. Phys.*, **25**, 1258 (1992).
15. Yu. E. Makushok, V. P. Parkhutik, J. M. Martinez-Duart, and J. M. Albella, *J. Phys. D: Appl. Phys.*, **27**, 661 (1994).
16. G. E. Thompson, R. C. Furneaux, and G. C. Wood, *Trans. Inst. Met. Finish.*, **57**, 123 (1979).
17. X. Zhang, M.S. Thesis, Iowa State University, Ames, IA (1996).
18. V. P. Parkhutik, *Corros. Sci.*, **26**, 295 (1986).
19. J. Scherer, O. M. Magnussen, T. Ebel, and R. J. Behm, *Corros. Sci.*, **41**, 35 (1999).
20. L. Chen and D. Guay, *J. Electrochem. Soc.*, **141**, L43 (1994).
21. L. Roué, L. Chen, and D. Guay, *Langmuir*, **12**, 5818 (1996).
22. P. Schmutz and G. S. Frankel, *J. Electrochem. Soc.*, **145**, 2295 (1998).
23. P. Schmutz and G. S. Frankel, *J. Electrochem. Soc.*, **146**, 4461 (1999).
24. T. Martin, X. Zhang, and K. R. Hebert, *J. Electrochem. Soc.*, To be published.
25. G. Patermarakis and N. Papandreadis, *Electrochim. Acta*, **38**, 2351 (1993).
26. F. Keller, M. S. Hunter, and D. L. Robinson, *J. Electrochem. Soc.*, **100**, 411 (1953).
27. T. P. Hoar and N. F. Mott, *J. Phys. Chem. Solids*, **9**, 97 (1959).
28. M. Nagayama and K. Tamura, *Electrochim. Acta*, **12**, 1097 (1967).
29. M. Nagayama, K. Tamura, and H. Takahashi, *Corros. Sci.*, **12**, 133 (1972).
30. C. Cherki and J. Siejka, *J. Electrochem. Soc.*, **120**, 784 (1973).
31. J. Siejka and C. Ortega, *J. Electrochem. Soc.*, **124**, 883 (1977).
32. T. Våland and K. E. Heusler, *J. Electroanal. Chem.*, **149**, 71 (1983).
33. G. C. Wood, P. Skeldon, G. E. Thompson, and K. Shimizu, *J. Electrochem. Soc.*, **143**, 74 (1996).
34. W. M. Deen, *Analysis of Transport Phenomena*, p. 34, Oxford, New York (1998).
35. W. W. Mullins, *J. Appl. Phys.*, **28**, 333 (1957).